

An eigenfunction-expansion method for predicting hydroelastic behavior of a shallow-draft VLFS

Jang Whan Kim and R. Cengiz Ertekin

Department of Ocean Engineering, SOEST, University of Hawaii at Manoa, 2540 Dole Street, Holmes Hall 402, Honolulu, HI 96822, USA. kju@oceaneng.soest.hawaii.edu, ertekin@hawaii.edu

ABSTRACT: A new method is developed to study the linear hydroelastic behavior of a rectangular airport or runway whose draft is “small” and which floats in finite depth of water. The numerical model employs the recently developed wavemaker theory for the fluid layer covered by a thin, elastic plate. The velocity potentials in regions with and without the plate is expanded by eigenfunctions in vertical mode which satisfy the governing equations and free-surface conditions, taking into account the presence of the floating elastic plate. The final equations are reduced to a set of integral equations to be solved along the edge of the plate by matching the solutions defined in the two regions and by enforcing the free-edge conditions for the plate. Applications are made to study the hydroelastic response of floating runways. The results are compared with the available experimental data and numerical calculations by others. The mean drift loads on the mat are also calculated by following Maruo’s far-field method.

1 INTRODUCTION

In limited water depth areas, mat-type structures must be considered as floating runways/airports because they can provide a very large deck space with relatively shallow draft and at a low cost. As a penalty for these advantages, mat-type structures are inherently flexible and can easily respond to ambient waves. If the deformations due to waves are not confined along the edges of the mat, the taking-off and landing operations on the runway may be affected unfavorably.

Various methods have been proposed by many to theoretically predict the hydroelastic response of mat-type structures to waves. To name a few, Wang et al (1997) used the ‘three-dimensional hydroelasticity theory’ and the Green function method to obtain the ‘dry modes’ and the hydrodynamic coefficients, which can effectively be replaced by the thin-plate theory and the ‘zero-draft Green function method’ for mat-type structures. Kashiwagi (1998a) used the ‘B-spline Galerkin scheme’ to improve the computational efficiency in the evaluation of the hydrodynamic coefficients, and Ohmatsu (1998) used the ‘eigenfunction expansion method.’ These methods are based on the ‘generalized mode’ approach (see e.g., Wu (1984) and Newman (1994)) in which the motion of the structure is described by six-degree-of-freedom rigid-body motions plus numerous flexible modes which are given as

either the natural modes in vacuo (‘dry modes’) or well-chosen interpolation functions. In the practical range of the incoming wavelength, which is about one one-hundredths of the mat length, the required number of modes is quite large as can be seen, for example, in the results of Kashiwagi (1998a). One may then easily argue that there is not much of an advantage in the use of the ‘generalized mode’ approach over the ‘direct method’ where the dynamic equations for the structure and fluid are coupled and solved numerically (see e.g., Mamidipudi & Webster (1994)). The recent study of Kashiwagi (1998b) shows that these two methods are equivalent to each other except the choice of the interpolation functions to describe the deformations of the structure.

Recently, there has been another line of approach to this problem. Ohkusu & Nanba (1996) showed that the presence of the elastic plate can be considered by modifying the free surface condition as in the capillary-gravity wave problem. In this approach, the floating plate and fluid beneath are treated as uniform media of hydroelastic waves on the horizontal plane and the waves on the plate are identified by only one wavelength for a given frequency; in turn this enables us to describe the deformation of the plate much more efficiently than the other approaches in which large number of modes are required. In fact, this approach has been widely used in the study of the elastic deformation

of ice floes in the arctic region (see, e.g., Stoker (1957), Evans & Davies (1968), Meylan & Squire (1994), Fox & Squire (1994)). Ohkusu & Namba (1998) employed Stoker's (1957) and Meylan & Squire's (1994) theories to investigate the hydroelastic response of an infinitely long plate in oblique waves in both shallow and deep waters. Kim & Ertekin (1998a) introduced the Green-Naghdi theory for the same problem in shallow waters. They showed that the Green-Naghdi theory provides equations similar to Stoker's but with an improved dispersion property. They also showed that the deflections along the center of the plate can be significant when the incidence angle of the incoming waves is close to the critical angle, which is defined as the minimum angle for which waves can be transmitted through the plate. Ertekin & Kim (1998) extended the theory to three dimensions successfully after factorizing the coupled fluid-plate equation into three Helmholtz equations, which are solved by the boundary integral equation (BIE) method. This method has been proved very efficient in the parametric study of the hydroelastic response of a mat-type floating runway in regular waves because, unlike in the usual panel methods which require the discretization of the entire mat, one needs to discretize the mat only along its edges so that the time-consuming evaluation of surface integrals is replaced by the evaluation of line integrals with much more efficiency.

In this paper, we combine the method of Ertekin & Kim (1998) devised for shallow water conditions and the two dimensional wavemaker theory for an elastic plate floating on water of finite depth, to develop a new method which can treat the hydroelastic response of a rectangular mat. The wavemaker theory is recently developed by Kim & Ertekin (1998b), where the completeness and orthogonality properties of the eigenfunctions in an hydroelastic problem are shown. Unlike in the fluid domain without the presence of the floating plate, the boundary value problem in this problem is not self-adjoint, as indicated by the existence of two complex-valued eigenfunctions shown by Evans & Davies (1968). As a result, the eigenfunctions are not orthogonal to each other and completeness of the eigenfunctions is not clear.

Kim & Ertekin (1998b) showed recently that the these undesirable properties are due to the redundancy in the eigenfunctions; that is, the two complex-valued eigenfunctions are linearly dependent on the other real-valued eigenfunctions from which we can build a minimal subset of the complete set. They also built another set of eigenfunctions, which is orthogonal to the real-valued eigenfunctions. Within the framework of their wavemaker theory, the solutions in the region with and without the floating plate can be expanded in terms of the eigenfunctions in vertical mode defined in each region and the coefficients of the eigenfunctions can be obtained from the continuity of normal velocity and pressure on the vertical surface along the edges of the

plate. This could effectively be done using the orthogonality properties of the eigenfunctions. The two coefficients of the redundant eigenfunctions in the plate region can be given in terms of the coefficients of the real-valued eigenfunctions using the free-edge conditions, which state the vanishing of shear force and bending moment along the edges of plate. This matching procedure is different from that of Fox & Squire (1994), where the matching was made using the least square method.

In the present method, the coefficients of the eigenfunctions in vertical mode satisfy the Helmholtz equations on the horizontal plane and we solve for them differently in the two regions. In Region II, we use the eigenfunction method and in Region I, we use BIE method. This procedure is similar in mathematical structure to the one devised by Yeung & Bouger (1979) who used the BIE method in the interior region and the eigenfunction method in the outer region to obtain the solution of the problem of steady two-dimensional ship waves.

The new method is applied to a 5-km long very large floating structure (VLFS) used by Kashiwagi (1998b). After showing the convergence of the numerical solution, the ranges of validity of shallow water wave theories are tested by comparison. Comparisons are also made with the numerical and experimental results obtained by Kashiwagi (1998a) and Ohta & Ohmatsu (1998), and good agreements are obtained. The present numerical method is so computationally efficient that we can survey various features of the hydroelastic response of the VLFS over a wide range of incoming wavelengths and incidence angles without any difficulty. And finally, the mean drift forces on the horizontal plane are calculated based on Maruo's (1960) far-field approach.

2 FORMULATION

An elastic mat of rectangular plan geometry, with length, L , and beam, B , is considered, see Fig. 1. The mat is freely floating on an inviscid fluid-layer of constant density, ρ , and depth, h , and is under the action of linear water waves of angular frequency, ω , and of angle, β . Two regions which describe the fluid region (I) and the fluid-plate region (II) are considered, and these regions are separated by the juncture boundary, J .

We assume that the wave amplitude, A , of the incoming waves is much smaller than the wavelength, $\lambda = 2\pi/k$, (or $kA \ll 1$), such that we can use the linear theory to model the motion of the fluid layer. We also assume that the thickness of the mat is much smaller than the length and beam of the mat so that we can employ the thin-plate theory that governs the hydroelastic deflections of the mat.

Within the scope of the linear theory, the motions of the plate and fluid can be assumed time harmonic

with the same frequency, ω , of the incoming waves. Hereafter, we will represent any time-harmonic function, say $F(x, y, z, t)$, as the real part of $f(x, y, z)e^{-i\omega t}$ by introducing a complex function, $f(x, y, z)$ that depends on the spatial variables only.

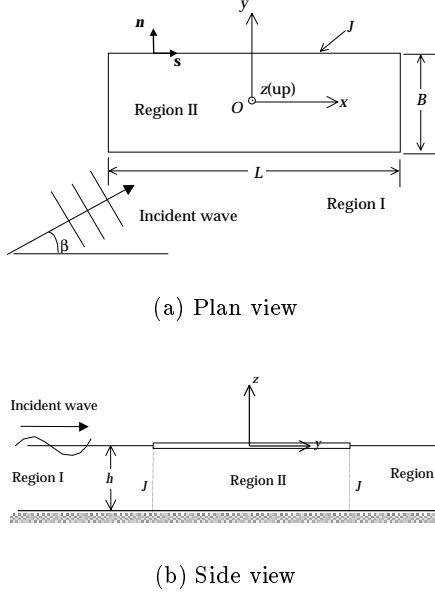


Fig. 1: Definition sketch of the problem.

The rectangular mat is assumed to have a uniform mass distribution (per unit area), m , and flexural rigidity (per unit width), $D = EI/B$, where E is Young's modulus and I is the moment of inertia of plate cross section. The vertical displacement, $\zeta(x, y)$, of the mat is assumed to be governed by the thin-plate theory (see e.g., Rayleigh (1894)):

$$-m\omega^2\zeta + D\Delta^2\zeta = p_f, \quad (1)$$

where $p_f = p_f(x, y)$ is the spatial part of the time-harmonic pressure on the lower surface of the plate and $\Delta = \partial^2/\partial x^2 + \partial^2/\partial y^2$ is the two-dimensional Laplacian on the horizontal plane.

Since the plate is freely floating, the bending moment and shear force should vanish at the edges of the plate, *i.e.*,

$$\frac{\partial^2\zeta}{\partial n^2} + \nu \frac{\partial^2\zeta}{\partial s^2} = 0, \quad \frac{\partial^3\zeta}{\partial n^3} + (2 - \nu) \frac{\partial^3\zeta}{\partial s^2\partial n} = 0 \quad \text{on } J, \quad (2)$$

where n and s denote the normal and tangential directions as seen in Fig. 1, and ν is Poisson's ratio. The equation (2) can alternatively be written on J as

$$\Delta\zeta - (1 - \nu) \frac{\partial^2\zeta}{\partial s^2} = 0, \quad \frac{\partial}{\partial n} \left\{ \Delta\zeta + (1 - \nu) \frac{\partial^2\zeta}{\partial s^2} \right\} = 0. \quad (3)$$

At the corners of the plate, there can be concentrated shear force to compensate for the torsional moment along the edges of the plate. The vanishing of

this shear force leads to

$$\frac{\partial^2\zeta}{\partial x\partial y} = 0 \quad \text{at } x = \pm \frac{L}{2} \quad \text{and } y = \pm \frac{B}{2}. \quad (4)$$

For the fluid motion, we assume that the fluid is inviscid and incompressible and its motion is irrotational. Then we can introduce the velocity potential, $\phi(x, y, z)$, by which the velocity field is defined as $\mathbf{u}(x, y, z) = \nabla\phi$. The velocity potential must satisfy the Laplace equation in the fluid domain:

$$\Delta\phi + \frac{\partial^2\phi}{\partial z^2} = 0, \quad -h < z < 0, \quad (5)$$

and the kinematic boundary conditions on the boundaries, *i.e.*,

$$\frac{\partial\phi}{\partial z}(x, y, -h) = 0, \quad (6)$$

$$\frac{\partial\phi}{\partial z}(x, y, 0) = -i\omega\zeta(x, y). \quad (7)$$

The dynamic boundary condition on the $z = 0$ plane can be written as

$$-i\omega\rho\phi(x, y, 0) + \rho g\zeta(x, y) = p_f(x, y). \quad (8)$$

In Region I, the pressure $p_f(x, y)$ is equal to the atmospheric pressure which is assumed to be negligible, and in Region II, it is unknown and is equal to the pressure on the right-hand side of (1).

The equations (1), (7) and (8) can be combined (see e.g., Evans & Davies (1968) and Meylan & Squire (1994)) as

$$(\rho g - m\omega^2 + D\Delta^2) \frac{\partial\phi}{\partial z} + \rho\omega^2\phi = 0 \quad \text{on } z = 0, \quad (9)$$

and the linear free-surface condition in Region I can simply be obtained by setting $m = D = 0$ in (9):

$$\frac{\partial\phi}{\partial z} + \frac{\omega^2}{g}\phi = 0, \quad z = 0. \quad (10)$$

Along the juncture boundary, J , the continuities of mass flux and depth-mean pressure lead to the following matching conditions:

$$\frac{\partial\phi_I}{\partial n} = \frac{\partial\phi_{II}}{\partial n}, \quad \phi_I = \phi_{II} \quad \text{on } J, \quad (11)$$

where ϕ_I and ϕ_{II} are the velocity potentials in Regions I and II, respectively.

The additional condition, namely the radiation condition, has to be imposed on part of ϕ_I ; this will be discussed in the following section.

3 METHOD OF SOLUTION

Since we neglected the nonlinearity of the free-surface conditions and the thickness of the plate, the fluid domain remains as a simple rectangular domain. As a result, the boundary-value problem given by (5)-(11)

can be solved by the separation of variables method. The solutions in Regions I and II can be represented by series of vertical modes, which can be written as the eigenfunctions of the eigenvalue problem defined on a one-dimensional, vertical water column between $z = -h$ and $z = 0$. The coefficients of the eigenfunctions are functions of (x, y) and should satisfy the two-dimensional equations.

The eigenfunctions in Region I are well known and their orthogonality property and completeness are well established (see Wehausen & Laitone (1960)). However, the eigenfunctions in Region II do not possess these features. The boundary-value problem in Region II is not self-adjoint due to the higher-order terms in the free-surface condition (9). As a result, the eigenfunctions are not real valued and orthogonal (see Evans & Davies (1968), Fox & Squire (1994), Kim & Ertekin (1998b)). However, as shown by Fox & Squire (1994), the eigenfunctions are complete and can be used to expand the solution in Region II in a series form. In fact, Kim & Ertekin (1998b) showed that the eigenfunction set is redundantly complete, *i.e.*, the subset containing the real-valued eigenfunctions is a minimally complete subset and the remaining two complex-valued eigenfunctions can be given as linear combinations of the other real-valued eigenfunctions.

Based on these properties of eigenfunctions, the solution in Region II is expanded in terms of an eigenfunction series in which the two redundant eigenfunction terms are used to satisfy the free-edge conditions in (3), and the others to satisfy the matching conditions in (11). The coefficients of the eigenfunctions are given as the solution of the Helmholtz equations in a rectangular domain.

3.1 Solution in Region I

The general solution in Region I can be expanded by the complete set of eigenfunctions $\{f_0(z), f_1(z), \dots\}$ (see Wehausen & Laitone (1960)) defined as

$$f_m(z) = \left(\frac{h}{2} + \frac{g}{2\omega^2} \sinh^2 k_m \right)^{-1/2} \cosh k_m(z + h), \quad (12)$$

where k_0 the real and k_1, k_2, \dots are the imaginary roots of the transcendental equation,

$$\omega^2 = gk \tanh kh. \quad (13)$$

The eigenfunctions are orthogonal, and are normalized such that

$$\int_{-h}^0 f_m(z) f_n(z) dz = \delta_{mn}, \quad (14)$$

where δ_{mn} is the Kronecker delta.

We write the general solution of ϕ_I in Region I as

$$\begin{aligned} \phi_I(x, y, z) = & -\frac{i\omega A}{f'_0(0)} f_0(z) e^{ik(x \cos \beta + y \sin \beta)} \\ & + \sum_{m=0}^{\infty} \phi_m(x, y) f_m(z), \end{aligned} \quad (15)$$

where prime denotes differentiation with respect to z , the first term on the right-hand side is the incident wave potential of amplitude A and incidence angle β and the remaining terms under the summation sign represent the diffraction and radiation potentials due to the presence of the freely floating plate.

The coefficients $\phi_m(x, y)$ satisfy the Helmholtz equations:

$$\Delta \phi_m + k_m^2 \phi_m = 0, \quad m = 0, 1, 2, \dots, \quad (16)$$

defined on the horizontal xy -plane. The solution of (16) for $m = 0$ is the wave solution, which represents waves that propagate to infinity. For $m \geq 1$, the solution represents the local disturbances trapped near the plate. The potentials, ϕ_m , must also satisfy the radiation condition, *i.e.*,

$$\sqrt{r} \left(\frac{\partial \phi_m}{\partial r} - ik_m \phi_m \right) = 0 \quad \text{as } r \rightarrow \infty. \quad (17)$$

The general solutions of (16) and (17) can be written in terms of boundary integrals along the contour C_J , which is defined as the projection of J on to the horizontal plane. If we use the source distribution of strength $\sigma_m(s)$, we can write

$$\phi_m(x, y) = \int_{C_J} \sigma_m(s) G_m(|\mathbf{x} - \boldsymbol{\xi}(s)|) ds, \quad (18)$$

where $\mathbf{x} = (x, y)$ is the field point and $\boldsymbol{\xi}(s) = (\xi(s), \eta(s))$ is the source point on C_J , and $G_m(r)$ are the Green functions given by

$$G_0(r) = \frac{\pi}{2i} H_0^{(1)}(k_0 r), \quad G_m(r) = -K_0(|k_m| r), \quad m \geq 1, \quad (19)$$

where $H_0^{(1)}$ is the Hankel function and K_0 is the modified Bessel function of the second kind.

The general solution given by (15) and (18) satisfies the Laplace equation (5), the free-surface condition (10) and the radiation condition (17). The solution can thus be obtained after the source strengths, $\sigma_m(s)$, are determined by matching the solution with that in Region II, and this will be discussed later.

3.2 Solution in Region II

The eigenfunctions in Region II and for $m = -2, -1, 0, \dots$ are given as

$$\varphi_m(z) = \left(\frac{h}{2} + \frac{\rho g - m\omega^2 + 5D\mu_m^4}{2\omega^2 \rho} \right)^{-1/2} \cosh \mu_m(z + h), \quad (20)$$

where the eigenvalues, μ_m , are the roots of

$$\omega^2 = g\mu \left(1 - \frac{m\omega^2}{\rho g} + \frac{D}{\rho g} \mu^4 \right) \tanh \mu h. \quad (21)$$

Here, we denote μ_{-2} and μ_{-1} as the complex eigenvalues on the 1st and 2nd quadrant of the complex μ -plane ($\mu_{-2} = -\mu_{-1}^*$), and μ_0 as the positive real root and μ_1, μ_2, \dots as the imaginary roots as seen in Fig. 2. The existence of the complex roots μ_{-2} and μ_{-1} is due to Evans & Davies (1968).

The functions $\varphi_m(z)$ given by (20) are real valued, except $\varphi_{-1}(z)$ and $\varphi_{-2}(z)$. As shown by Kim & Ertekin (1998b), φ_{-1} and φ_{-2} can be written as linear combination of the real valued eigenfunctions $\varphi_0, \varphi_1, \dots$, *i.e.*,

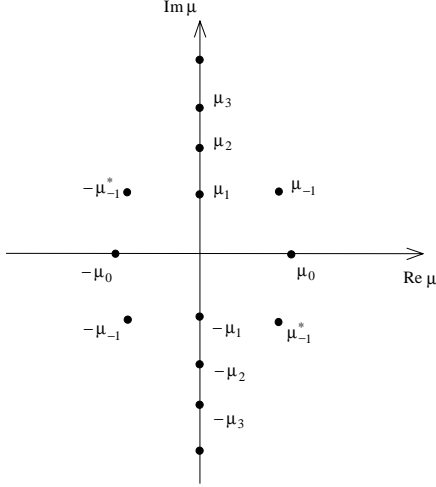


Fig. 2: Eigenvalues of the hydroelastic problem.

$$\varphi_{-1}(z) = \sum_{m=0}^{\infty} \alpha_m \varphi_m(z), \quad \varphi_{-2}(z) = \sum_{m=0}^{\infty} \alpha_m^* \varphi_m(z), \quad (22)$$

where

$$\alpha_m \equiv - \frac{\mu_{-1}^{*2} - \mu_m^2}{\mu_{-1}^{*2} - \mu_{-1}^2} \frac{\varphi_m'(0)}{\varphi_{-1}'(0)}, \quad (23)$$

where asterisk denotes complex conjugate. It has also been shown that the real-valued eigenfunctions are complete and orthogonal to another set, $\{\varphi_m^c(z), m = 0, 1, \dots\}$, *i.e.*,

$$\int_{-h}^0 \varphi_m(z) \varphi_n^c(z) dz = \delta_{mn}, \quad (24)$$

where

$$\varphi_m^c(z) \equiv 2\Re \{\alpha_m \varphi_{-1}(z)\} + \varphi_m(z), \quad m = 0, 1, \dots \quad (25)$$

The general solution in Region II can now be written as

$$\phi_{II}(x, y, z) = \sum_{m=-2}^{\infty} \psi_m(x, y) \varphi_m(z), \quad (26)$$

where the coefficients, $\psi_m(x, y)$, are the solutions of

$$\Delta \psi_m + \mu_m^2 \psi_m = 0, \quad m = -2, -1, 0, \dots \quad (27)$$

Since the Helmholtz equations in (27) are defined in a bounded rectangular region, we can represent the general solution as the sum of the eigenfunctions and adopt the representation used by Ertekin & Kim (1998):

$$\begin{aligned} \psi_m(x, y) = & \sum_{n=0}^{\infty} \left[\{a_{mn} e^{-\gamma_{mn}^y (B/2+y)} \right. \\ & + b_{mn} e^{-\gamma_{mn}^y (B/2-y)} \} \cos(\lambda_m^x (x + L/2)) \\ & + \{c_{mn} e^{-\gamma_{mn}^x (L/2+x)} \\ & + d_{mn} e^{-\gamma_{mn}^x (L/2-x)} \} \cos(\lambda_m^y (y + B/2)) \Big], \end{aligned} \quad (28)$$

where

$$\begin{aligned} \lambda_m^x &= \frac{m\pi}{L}, \quad \lambda_m^y = \frac{m\pi}{B}, \\ \gamma_{mn}^y &= \sqrt{(\lambda_{mn}^x)^2 - \mu_m^2}, \quad \Re\{\gamma_{mn}^y\} \geq 0, \\ \gamma_{mn}^x &= \sqrt{(\lambda_{mn}^y)^2 - \mu_m^2}, \quad \Re\{\gamma_{mn}^x\} \geq 0. \end{aligned} \quad (29)$$

The coefficients a_{mn}, b_{mn}, c_{mn} and d_{mn} can be obtained from coefficients of the Fourier cosine transformation of the normal gradient, $\partial \phi_m / \partial n$, on C_J (see Ertekin & Kim (1998)).

As a result, we have represented the solutions in Regions I and II by using $\sigma_m(s)$ and $\frac{\partial \psi_m}{\partial n}(\xi(s), \eta(s))$ as parameters. These parameters can be determined from the matching conditions (11) and the free-edge conditions (3), which will be discussed next.

3.3 Matching conditions

Using the representations (15) and (26), the matching conditions in (11) can be written as

$$\sum_{m=-2}^{\infty} \frac{\partial \psi_m}{\partial n} \varphi_m(z) = \sum_{m=0}^{\infty} \frac{\partial \phi_m}{\partial n} f_m(z) + \frac{\partial \phi_w}{\partial n} \delta_{m0}, \quad (30a)$$

$$\sum_{m=-2}^{\infty} \psi_m \varphi_m(z) = \sum_{m=0}^{\infty} \phi_m f_m(z) + \phi_w f_0(z) \quad \text{on } J, \quad (30b)$$

where ϕ_w is the coefficient of the eigenfunction $f_0(z)$ for the incoming potential, *i.e.*,

$$\phi_w = - \frac{i\omega A}{f_0'(0)} e^{ik(x \cos \beta + y \sin \beta)}. \quad (31)$$

By taking the inner products of the matching conditions, (30), with the orthonormal basis $\{f_m(z), m = 0, 1, \dots\}$, we can obtain the following equations for $m = 0, 1, 2, \dots$:

$$\sum_{n=-2}^{\infty} \Psi_{mn} \frac{\partial \psi_m}{\partial n} - \frac{\partial \phi_m}{\partial n} = \frac{\partial \phi_w}{\partial n} \delta_{m0}, \quad (32a)$$

$$\sum_{n=-2}^{\infty} \Psi_{mn} \psi_n - \phi_m = \phi_w \delta_{m0} \quad \text{on } C_J, \quad (32b)$$

where

$$\Psi_{mn} \equiv \int_{-h}^0 f_m(z) \varphi_n(z) dz. \quad (33)$$

Note that, we could also have used the other complete set in (25), $\{\varphi_m^c(z), m = 0, 1, 2, \dots\}$, when we projected (30) onto C_J . If we have done that, we could have written (for $m = 0, 1, 2, \dots$)

$$\sum_{n=-2}^{-1} \Psi_{mn}^c \frac{\partial \psi_m}{\partial n} + \frac{\partial \psi_m}{\partial n} - \sum_{n=0}^{\infty} \Phi_{mn}^c \frac{\partial \phi_m}{\partial n} = \Phi_{m0}^c \frac{\partial \phi_w}{\partial n}, \quad (34a)$$

$$\sum_{n=-2}^{-1} \Psi_{mn}^c \psi_m + \psi_m - \sum_{n=0}^{\infty} \Phi_{mn}^c \phi_m = \Phi_{m0}^c \phi_w, \quad \text{on } C_J, \quad (34b)$$

where

$$\Psi_{mn}^c \equiv \int_{-h}^0 \varphi_m^c(z) \varphi_n(z) dz, \quad \Phi_{mn}^c \equiv \int_{-h}^0 \varphi_m^c(z) f_n(z) dz, \quad (35)$$

instead of (32). The expressions in (34) are more complicated and thus will not be used here; however, whenever there is a discontinuity in the thickness of the fluid domain, e.g., when the nonzero-draft of the plate is considered, we have to use (32a) and (34b) as the matching conditions for the continuity of mass flux and pressure, respectively. In that case, the limits of the definite integral in (35) should also be changed to $(-h, -d)$, where d is the draft.

When we truncate the infinite series in (15) and (26) at a finite number of terms, say M , we have $2M + 2$ unknown functions, $\{\phi_m(x, y), m = 0, 1, \dots, M\}$ and $\{\psi_m(x, y), m = -2, -1, 0, 1, \dots\}$, whereas we have $2M$ matching conditions given in (32) (or in (34)). The additional two equations can be obtained from the free-edge conditions given in (3).

The deflections of the plate, $\zeta_{II}(x, y)$, can be obtained from (17) and (26) as

$$\zeta_{II}(x, y) = \frac{i}{\omega} \sum_{m=-2}^{\infty} \varphi'_m(0) \psi_m(x, y). \quad (36)$$

Then the free-edge conditions given in (3) can be written on C_J as

$$\begin{aligned} \sum_{m=-2}^{\infty} \left[\phi'_m(0) \left\{ \mu_m^2 + (1 - \nu) \frac{\partial^2}{\partial s^2} \right\} \psi_m \right] &= 0, \\ \sum_{m=-2}^{\infty} \left[\phi'_m(0) \left\{ \mu_m^2 - (1 - \nu) \frac{\partial^2}{\partial s^2} \right\} \frac{\partial \psi_m}{\partial n} \right] &= 0. \end{aligned} \quad (37)$$

Note that the corner condition (4) is already satisfied by the general solution given in (28), and this can be shown by using (36).

3.4 Discretization

To consider the conditions along the mat edge, (32) and (37), numerically, we truncate the infinite series (15), (26) and (28) at a finite number of terms and use the constant panel method to solve the line integral (18). At first, we truncate the number of eigenfunctions at M :

$$\phi_I(x, y, z) = \phi_w f_0(z) + \sum_{m=0}^M \phi_m(x, y) f_m(z), \quad (38)$$

$$\phi_{II}(x, y, z) = \sum_{m=0}^M \psi_m(x, y) \varphi_m(z). \quad (39)$$

Then we divide the contour C_J into a finite number of intervals, I_1, I_2, \dots, I_{N_p} , as shown in Fig. 3. The arclength coordinate s is defined such that it starts from $s = 0$ at the upper left corner ($x = -L/2, y = B/2$) and ends at $s = 2(L + B)$ at the same corner, moving in the clockwise direction. We also denote the length of the segment I_i by h_i , and the coordinates of the middle of the panel by $\mathbf{x}_i = (x_i, y_i)$.

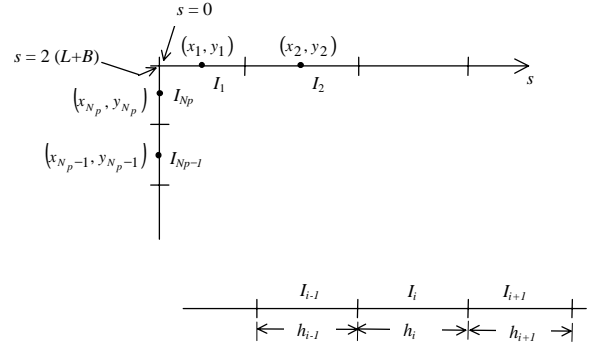


Fig. 3: Mesh system around the upper left corner.

The source strength, $\sigma_m(s)$, in (18) can be approximated as a piecewise constant function on C_J :

$$\sigma_m(s) = \mathbf{N}^T(s) \boldsymbol{\sigma}_m, \quad (40)$$

where $\boldsymbol{\sigma}_m = \{\sigma_{m1}, \sigma_{m2}, \dots, \sigma_{mN_p}\}^T$, $m = 0, 1, \dots, M$, are the column vectors of the nodal values of σ_m on each segment and $\mathbf{N}(s) = \{N_1(s), N_2(s), \dots, N_{N_p}(s)\}^T$ is that of piecewise constant interpolation functions defined as

$$N_i(s) = \begin{cases} 1, & s \in I_i, \\ 0, & \text{otherwise.} \end{cases} \quad (41)$$

Substituting (40) in (18), we obtain

$$\phi_m(x, y) = \int_{C_J} G_m(|\mathbf{x} - \boldsymbol{\xi}(s)|) \mathbf{N}^T \boldsymbol{\sigma}_m ds. \quad (42)$$

The functions, $\psi_m(x, y)$, $m = -2, -1, 0, \dots$, are approximated by truncating the infinite series (28) at

$M_x + 1$ and $M_y + 1$ cosine modes in the x and y directions, respectively. For convenience, we relabel the eigenfunctions and their coefficients to define the following column vectors, ϵ_m and $\mathbf{H}_m(x, y)$:

$$\epsilon_m = \left\{ a_{m0}, \dots, a_{mM_x}; b_{m0}, \dots, b_{mM_x}; c_{m0}, \dots, c_{mM_y}; d_{m0}, \dots, d_{mM_y} \right\}^T, \quad (43)$$

$$\mathbf{H}_m(x, y) = \left\{ e^{-\gamma_{m0}^y(B/2+y)} \cos(\lambda_0^x(x+L/2)), \dots, e^{-\gamma_{mM_x}^y(B/2+y)} \cos(\lambda_{M_x}^x(x+L/2)); \dots; e^{-\gamma_{m0}^x(L/2+x)} \cos(\lambda_0^y(y+B/2)), \dots, e^{-\gamma_{mM_y}^x(L/2+x)} \cos(\lambda_{M_y}^y(y+B/2)) \right\}^T. \quad (44)$$

We also define a column vector $\mathbf{C}(s)$ of cosine modes along the edges of the plate:

$$\mathbf{C}(s) = \left\{ \gamma_1(s), \dots, \gamma_{M_x}(s); \kappa_1(s), \dots, \kappa_{M_x}(s); \iota_1(s), \dots, \iota_{M_y}(s); \chi_1(s), \dots, \chi_{M_y}(s) \right\}^T, \quad (45)$$

where

$$\begin{aligned} \gamma_m(s) &= \begin{cases} \cos\{\lambda_m^x(2L+B-s)\}, & L+B < s < 2L+B, \\ 0, & \text{otherwise,} \end{cases} \\ \kappa_m(s) &= \begin{cases} \cos\{\lambda_m^x s\}, & 0 < s < L, \\ 0, & \text{otherwise,} \end{cases} \\ \iota_m(s) &= \begin{cases} \cos\{\lambda_m^y(s-2L-B)\}, & 2L+B < s < 2(L+B), \\ 0, & \text{otherwise,} \end{cases} \\ \chi_m(s) &= \begin{cases} \cos\{\lambda_m^y(L+B-s)\}, & L < s < L+B, \\ 0, & \text{otherwise.} \end{cases} \end{aligned} \quad (46)$$

Then, $\psi_m(x, y)$ can be written as

$$\psi_m(x, y) = \mathbf{H}_m(s) \epsilon_m. \quad (47)$$

Substituting (47) into the free-edge conditions (37) and taking the inner products of the equations with the cosine modes given in (45), we obtain

$$\mathbf{M}_{-1} \epsilon_{-1} + \mathbf{M}_{-1}^* \epsilon_{-2} = - \sum_{m=0}^M \mathbf{M}_m \epsilon_m, \quad (48a)$$

$$\mathbf{S}_{-1} \epsilon_{-1} + \mathbf{S}_{-1}^* \epsilon_{-2} = - \sum_{m=0}^M \mathbf{S}_m \epsilon_m, \quad (48b)$$

where the square matrices \mathbf{M}_m and \mathbf{S}_m are defined as

$$\mathbf{M}_m = \varphi'_m(0) \int_{C_J} \mathbf{C}(s) \left\{ \mu_m^2 + (1-\nu) \frac{\partial^2}{\partial s^2} \right\} \mathbf{H}_m^T ds, \quad (49a)$$

$$\mathbf{S}_m = \varphi'_m(0) \int_{C_J} \mathbf{C}(s) \left\{ \mu_m^2 - (1-\nu) \frac{\partial^2}{\partial s^2} \right\} \frac{\partial}{\partial n} \mathbf{H}_m^T ds. \quad (49b)$$

Using (48), we can represent ϵ_{-1} and ϵ_{-2} in terms of ϵ_m , $m \geq 0$:

$$\epsilon_{-1} = \sum_{m=0}^M \mathbf{A}_m \epsilon_m, \quad \epsilon_{-2} = \sum_{m=0}^M \mathbf{A}_m^* \epsilon_m, \quad (50)$$

where

$$\begin{aligned} \mathbf{A}_m &\equiv \left[(\mathbf{M}_{-1}^*)^{-1} \mathbf{M}_{-1} - (\mathbf{S}_{-1}^*)^{-1} \mathbf{S}_{-1} \right]^{-1} \cdot \\ &\quad \left[(\mathbf{S}_{-1}^*)^{-1} \mathbf{S}_m - (\mathbf{M}_{-1}^*)^{-1} \mathbf{M}_m \right]. \end{aligned} \quad (51)$$

The mass flux matching condition (32a) can be discretized in a similar manner. To do this, we substitute (42) and (47) into (32a) and take the inner product with the cosine modes to obtain the following equations for $m = 0, 1, 2, \dots, M$:

$$\sum_{n=-2}^M \Psi_{mn} \mathbf{F}_n^{II} \epsilon_n - \mathbf{F}_m^I \sigma_m = \delta \phi_w \delta_{m0}, \quad (52)$$

where

$$\mathbf{F}_m^I = \int_{C_J(s)} \mathbf{C}(s) \int_{C_J(\tau)} \frac{\partial G_m}{\partial n} (|\boldsymbol{\xi}(s) - \boldsymbol{\xi}(\tau)|) \mathbf{N}^T(\tau) d\tau ds, \quad (53a)$$

$$\mathbf{F}_m^{II} = \int_{C_J(s)} \mathbf{C}(s) \frac{\partial \mathbf{H}_m^T(s)}{\partial n} ds, \quad (53b)$$

$$\delta \phi_w = \int_{C_J(s)} \mathbf{C}(s) \frac{\partial \phi_w}{\partial n} ds. \quad (53c)$$

On the other hand, the pressure matching condition (32b), which is satisfied at the middle of the panels, I_1, I_2, \dots, I_{N_p} , becomes (after substituting (42) and (47) in (32b)):

$$\sum_{n=-2}^M \Psi_{mn} \mathbf{E}_n^{II} \epsilon_n - \mathbf{E}_m^I \sigma_m = \phi_w \delta_{m0}, \quad (54)$$

where

$$\mathbf{E}_m^I \equiv \begin{bmatrix} \mathbf{H}_m^T(x_1, y_1) \\ \mathbf{H}_m^T(x_2, y_2) \\ \vdots \\ \mathbf{H}_m^T(x_{N_p}, y_{N_p}) \end{bmatrix} \quad (55a)$$

$$\mathbf{E}_m^{II} \equiv \begin{bmatrix} \int_{C_J} G_m(|\mathbf{x}_1 - \boldsymbol{\xi}(s)|) \mathbf{N}^T(s) ds \\ \int_{C_J} G_m(|\mathbf{x}_2 - \boldsymbol{\xi}(s)|) \mathbf{N}^T(s) ds \\ \vdots \\ \int_{C_J} G_m(|\mathbf{x}_{N_p} - \boldsymbol{\xi}(s)|) \mathbf{N}^T(s) ds \end{bmatrix} \quad (55b)$$

$$\boldsymbol{\phi}_w = \left\{ \phi_w(x_1, y_1), \dots, \phi_w(x_{N_p}, y_{N_p}) \right\}^T. \quad (55c)$$

By using the relations given by (50), the algebraic equations (52) and (54) can be written as

$$\sum_{n=0}^M \left[\left(2\Re \left\{ \Psi_{m,-1} \mathbf{F}_{-1}^{II} \mathbf{A}_n \right\} + \Psi_{mn} \mathbf{F}_n^{II} \right) \boldsymbol{\epsilon}_n \right] - \mathbf{F}_m^I \boldsymbol{\sigma}_m = \delta \boldsymbol{\phi}_w \delta_{m0}, \quad m = 0, 1, \dots, M, \quad (56)$$

$$\sum_{n=0}^M \left[\left(2\Re \left\{ \Psi_{m,-1} \mathbf{E}_{-1}^{II} \mathbf{A}_n \right\} + \Psi_{mn} \mathbf{E}_n^{II} \right) \boldsymbol{\epsilon}_n \right] - \mathbf{E}_m^I \boldsymbol{\sigma}_m = \boldsymbol{\phi}_w \delta_{m0}, \quad m = 0, 1, \dots, M, \quad (57)$$

where \mathbf{F}_{-1}^{II} and \mathbf{E}_{-1}^{II} are defined similar to (53b) and (55b), respectively.

The total number of unknowns in (56) and (57) is $(M+1)\{2(M_x + M_y + 2) + N_p\}$, and we have $2(M+1)(M_x + M_y + 2)$ equations from (56) and $(M+1)N_p$ equations from (57).

3.5 Drift forces

The far-field integral representation of the second-order mean drift forces on the horizontal plane can be written in terms of the Kochin function that describes the far-field behavior of a disturbed wave system (Maruo 1960). We follow Mei (1992) (Art. 7.10) to write the drift force components in the x and y directions, respectively, as

$$\begin{aligned} \overline{F}_x(\beta) &= \frac{\rho g A^2}{\pi k} \frac{c_g}{c} \int_0^{2\pi} (\cos \beta - \cos \theta) |\mathcal{A}(\theta)|^2 d\theta, \\ \overline{F}_y(\beta) &= \frac{\rho g A^2}{\pi k} \frac{c_g}{c} \int_0^{2\pi} (\sin \beta - \sin \theta) |\mathcal{A}(\theta)|^2 d\theta, \end{aligned} \quad (58)$$

where $\mathcal{A}(\theta)$ is the complex, far-field wave amplitude function (or Kochin function) that is defined as

$$\mathcal{A}(\theta) = \frac{f_0'(0)}{4\omega} \int_{C_J} \left(\phi_0 \frac{\partial}{\partial n} - \frac{\partial \phi_0}{\partial n} \right) e^{ik(\xi(s) \cos \theta + \eta(s) \sin \theta)} ds. \quad (59)$$

The ratio between the group velocity and wave celerity for the linear theory is given by

$$\frac{c_g}{c} = \frac{1}{2} \left(1 + \frac{2kh}{\sinh 2kh} \right). \quad (60)$$

3.6 Irregular frequencies

Since the source distribution given by (18) for $m = 0$ can also describe the wave motion in the closed rectangular domain inside J , the source strength $\sigma(s)$ may not be unique at irregular frequencies which are eigenfrequencies of the interior flow (see John (1950) and Art. 7.8.2 of Mei (1992)). As a result, the algebraic equations (56) and (57) become ill-conditioned at these frequencies and this, in turn, causes very slow convergence of the numerical solution, as well as saw-tooth behavior in the results, especially of drift forces.

As a practical remedy, we introduce an artificial damping factor δ and modify the Green function in (19) as

$$G_0(r) = \frac{\pi}{2i} H_0^{(1)}(k_0(1+i\delta)r). \quad (61)$$

The optimal value of $\delta = 0.01$ was chosen such that it is large enough to prevent the algebraic equations (56) and (57) from being ill-conditioned and, at the same time, without affecting the solution significantly. Other values of δ , such as 0.001, was determined to be too small to have an appreciable effect, and a larger value, such as 0.1, introduced too much artificial damping in the results. An example that shows the effect of damping will be given later.

4 NUMERICAL RESULTS and DISCUSSION

The theory and the numerical method described in the preceding sections have been coded and applied to a number of problems studied by others. We first discuss the convergence and efficiency of the present method and then compare the present results with the ones studied by Kashiwagi (1998a) and (1998b), Ohta & Ohmatsu (1998) and Ohmatsu (1998). Comparisons are also made with the numerical results based on Stoker's shallow water wave theory and Green-Naghdi theory to verify their ranges of validity.

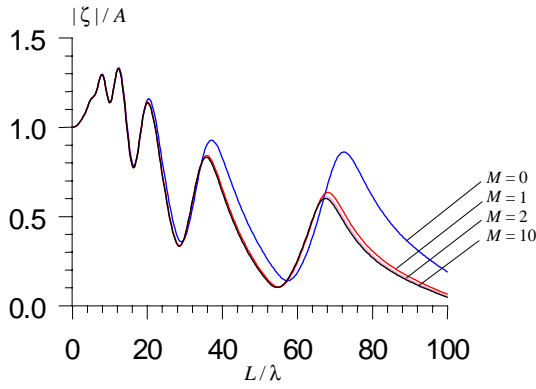
4.1 Convergence, accuracy and efficiency

We have studied the convergence, accuracy and efficiency of the present numerical method by considering the floating runway considered by Kashiwagi (1998a). The main dimensions, water depth and the material properties are given as $L = 5$ km, $B = 1$ km, $d = 5$ m, $h = 50$ m, $D = 1.96 \times 10^{11}$ N-m. The convergence of results is studied on the number of vertical modes, M , number of cosine modes M_x and M_y , and number of panels N_p .

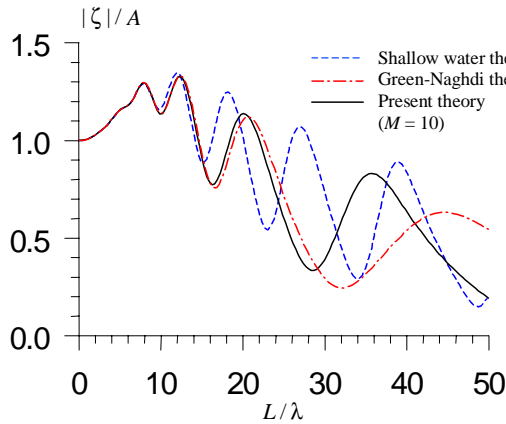
4.1.1 Convergence of results in M

The convergence of the results by increasing the number of eigenfunctions, M , is studied by using the two-dimensional beam sea model given in Kim & Ertekin (1998b). The length of the incoming waves,

λ , is varied from 50 m (or $L/\lambda = 100$) to infinity (or $L/\lambda = 0$). The wave period for $L/\lambda = 100$ is about 5.7 s. Note that the length of the runway is taken as infinitely long in the computations and $\beta = 90^\circ$. In Fig. 4(a), the deflection amplitude (per wave amplitude) at $y = -B/2$ is shown. As can be seen, the convergence in M is very fast. It seems that $M = 1$ is adequate to obtain a satisfactory solution within “engineering accuracy” when $L/\lambda < 70$, or when the wave period is longer than about 6.8 sec. The results for $M > 2$ are almost indistinguishable in the given wavelength range.



(a) Effect of M on the deflection amplitude



(b) Deflection amplitude comparison

Fig. 4: Plate deflection at $y = -B/2$, $\beta = 90^\circ$.

4.1.2 Comparative Accuracy

In Fig. 4(b), the converged results based on the present theory are compared with those obtained here by using the shallow water theory of Stoker (1957) and the Green-Naghdi theory, and by reproducing the schemes described in Ohkusu & Namba (1998) and Kim & Ertekin (1998a), respectively. Both approximate theories show good agreement with the present results for long waves. The range of validity of the Green-Naghdi theory looks greater than that of the shallow water theory and both methods predict the magnitude of deflections well, and the errors are mainly due to

the phase lag caused by dispersion errors in each of these theories (also see the comparisons given in Kim & Ertekin (1998a)).

4.1.3 Convergence of results in M_x , M_y , N_p

To determine the adequate number of panels that must be considered for accurate results, we studied the effect of different number of cosine modes in Region II and panels along the edges of the plate. In the following results, the number of panels, N_p , is maintained as four times the total number of cosine modes, *i.e.*, $2(M_x + M_y)$, which is proven to provide high accuracy and less computational time from numerical experiments. Fig. 5 shows the convergence of the plate deflection amplitude (along its edges) as a function of the number of panels for the same mat and for $\beta = 0^\circ$, $L/\lambda = 20$, $h = 50$ m. It is seen that the deflections converge uniformly as the number of panels increases. Comparison of these results with the ones based on the Green-Naghdi theory (Ertekin & Kim 1998) shows that the same order of convergence is reached in the present theory with less number of panels used. However, we found that the same order of convergence can be achieved if one replaces the constant-panel method of Ertekin & Kim (1998) by the eigenfunction expansion given by (28) to solve the Helmholtz equation in Region II. It appears that $N_p = 576$ produces sufficiently accurate results.

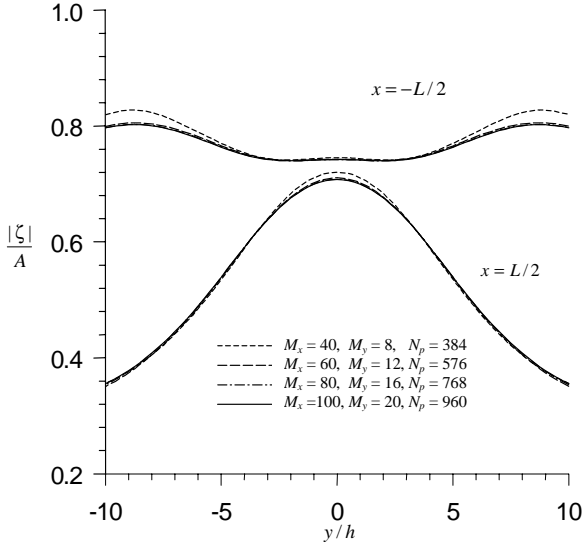
Table 1: CPU time for one frequency and one wave angle. Values in parentheses are those for an additional wave angle.

M_x, M_y, N_p	CPU time		
	$M = 0$	$M = 1$	$M = 2$
40, 8, 384	29 s (3 s)	56 s (3 s)	1 min 58 s (3 s)
80, 16, 768	2 min 3 s (7 s)	5 min 25 s (8 s)	13 min 14 s (9 s)
120, 24, 1152	5 min 8 s (12 s)	16 min 2 s (14 s)	41 min 42 s (17 s)

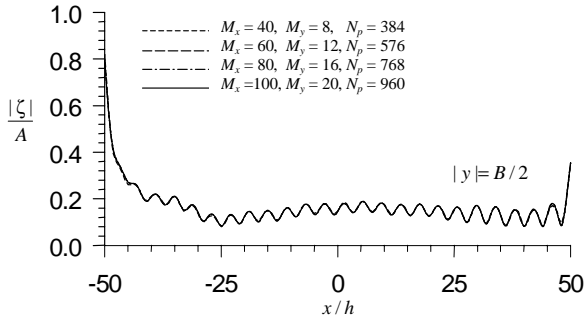
4.1.4 CPU time

The CPU time required to do the calculations on an IBM/RS6000/595 workstation are shown in Table 1 as a function of the number of panels along the longitudinal and transverse edges of the plate and the total number of panels used, and the number of eigenfunctions, M . It is seen that the increase in the CPU time varies quadratically with the total number of panels, N_p , and each additional eigenfunction effectively doubles the CPU time. The CPU time for an additional wave angle (shown in parentheses) is clearly much less. It is noted that these CPU times can further be reduced if one makes use of the fact that the mat geometry is

doubly symmetric with respect to the Oxz and Oyz planes. And as such, the double composite singularity distribution method (see Wu et al (1993)) can be employed.



(a) Leading and trailing edges



(b) Side edges

Fig. 5: Convergence of deflection, $L/\lambda = 20$.

4.1.5 The effect of artificial damping

The effect of artificial damping introduced in Section 3.6 is studied to determine the optimal value of δ . Fig. 6 shows the deflection RAO at the lower left corner of the plate in quartering seas ($\beta = 45^\circ$), and for the mat used by Kashiwagi (1998a) with $M_x = 40, M_y = 8, N_p = 384$. The effect of the damping factor δ near an irregular frequency can be seen in this figure.

4.2 Comparison with other results

The converged deflections for Kashiwagi's (1998a) model is compared with his results (obtained by the B-Spline Galerkin method) and with the Green-Naghdi theory results (Ertekin & Kim 1998) in Fig. 7 which shows the deflections along the edges of the mat and again for $\beta = 0^\circ$, $L/\lambda = 20$ and $h = 50$ m.

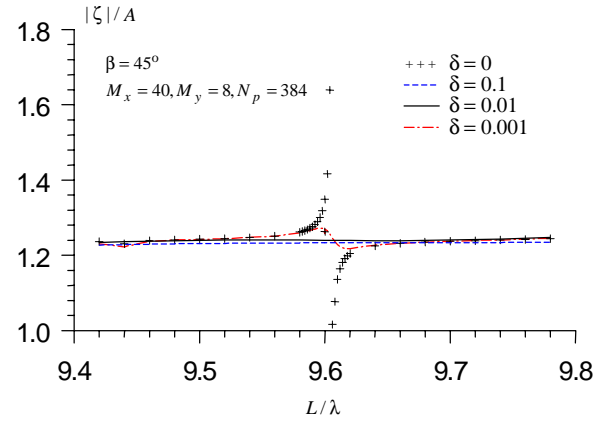
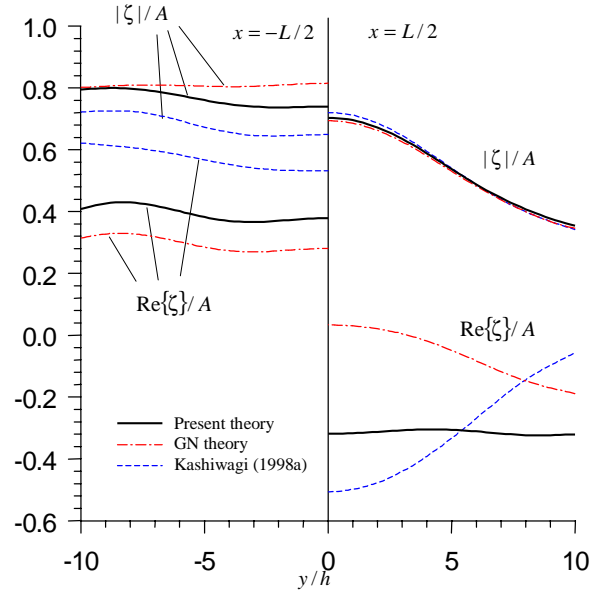
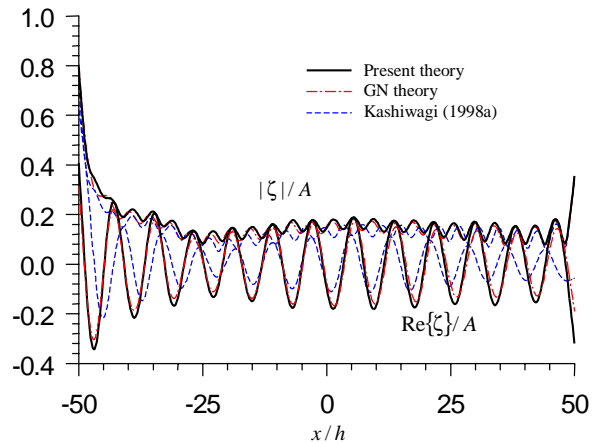


Fig. 6: The effect of the artificial damping on the deflection RAO near an irregular frequency.



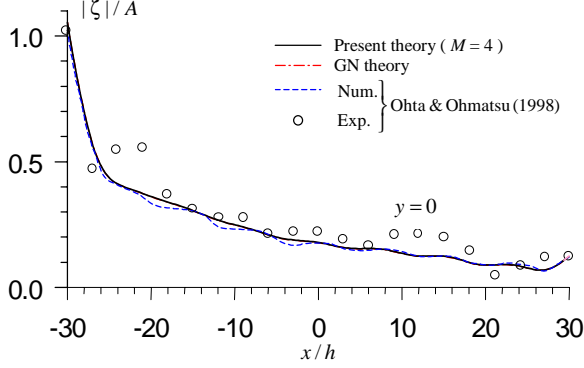
(a) Leading and trailing edges



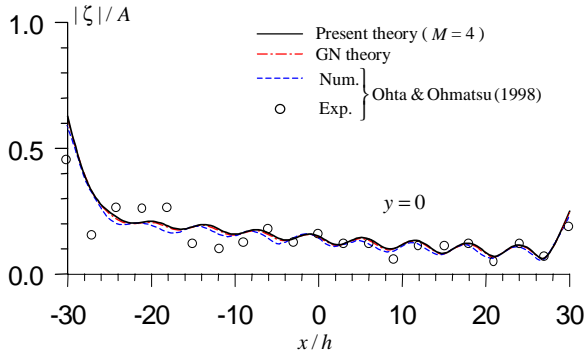
(b) Side edges

Fig. 7: Comparison with Kashiwagi's (1998a) and Ertekin & Kim's (1998) plate deflection results.

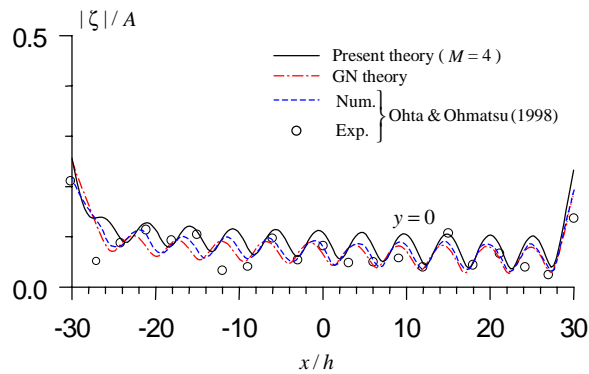
Along the side edges ($y = \pm B/2$), the deflection amplitudes calculated by the present method and by Ertekin & Kim (1998) and Kashiwagi (1998b) agree well although there are some differences in phase. Along the leading edge ($x = -L/2$), however, the GN theory predicts somewhat higher amplitude than the present theory along the center of the plate. The three amplitude predictions agree very well along the trailing edge ($x = L/2$) but with a phase difference again.



(a) $\lambda/L = 0.18$



(b) $\lambda/L = 0.10$



(c) $\lambda/L = 0.05$

Fig. 8: Comparisons with Ohta & Ohmatsu's (1998) and Ertekin & Kim's (1998) for three L/λ ratios.

As a second comparison, we consider the experimental and numerical results of Ohta and Ohmatsu (1998) obtained for a prototype runway ("VLFS15" model) and the Green-Naghdi results obtained for the same structure by Ertekin & Kim (1998). The specifications of the model are given as $L = 1.2$ km, $B = 240$ m, $d = 1$ m, $D = 4.46 \times 10^{10}$ N-m, $h = 20$ m, $\nu = 0.3$.

We show the comparisons of deflection amplitudes along the centerline, $y = 0$, in Fig. 8, where circles denote the experimental data of Ohta and Ohmatsu (1998). Three ratios of $\lambda/L = 0.18, 0.10, 0.05$ are considered in Fig. 8. The agreement among the present numerical results, Green-Naghdi theory results (Ertekin & Kim 1998) and Ohta and Ohmatsu's numerical results based on the 3-dimensional potential theory is overall very good. It is noted that the present results based on the linear potential theory predict higher deflection amplitudes for the $\lambda/L = 0.05$ case, in which the wave length is not very "long," and the ratio of $\lambda/h = 3$ for this case indicates that the finite-water depth effect is strong. Nevertheless, the discrepancies between the present and Ohta and Ohmatsu's results for $\lambda/L = 0.05$ are not well understood because both theories are based on the three-dimensional potential theory; the differences may be due to the particular discretization schemes used.

4.2.1 Effect of wave angle

We also studied the effect of wave angle on the hydroelastic response and drift forces. To do this, we again consider the 5-km-long runway of Kashiwagi (1998a) for the wavelength of 125 m ($L/\lambda = 40$); the corresponding wave period is about 9 s. The amplitudes of deflection at the four corners of the mat are shown in the top graph of Fig. 9 as functions of the wave angle. The middle graph shows the maximum deflection and slope of the runway along the centerline of the mat ($|x| < 0.25L$, $y = 0$). And the bottom graph shows the mean drift forces in both the x and y directions.

The two vertical lines in these figures indicate the "critical angles," β_c (for the side edge, $y = -B/2$) and $90^\circ - \beta_c$ (for the leading edge, $x = -L/2$), where the critical angle β_c is defined as the wave angle for which the transmitted hydroelastic-wave angle on the mat is zero. This angle is a result of Snell's law, see e.g., Kim & Ertekin (1998a) and Iwahashi et al (1998).

As can be seen in Fig. 9, the hydroelastic response changes dramatically with β . The wave length is sufficiently shorter than the plate width in this case and, as a result, waves cannot be transmitted through the longitudinal edge, $y = -B/2$, when $\beta < \beta_c$. Similarly, when $\beta > (90^\circ - \beta_c)$, waves cannot be transmitted through the leading edge, $x = -L/2$. It is also seen that the results become maximum at or near the critical angle. The deflection (nondimensionalized with re-

spect to the incoming wave amplitude) at the lee side, $y = B/2$, increases when $\beta > \beta_c$. The maximum deflection and the slope along the centerline of the mat also increase for $\beta > \beta_c$. It is clear that the best conditions for the take-off and landing of an aircraft are achieved when the wave angle is between $30^\circ - 60^\circ$. It is noted that the present results are very similar to the Green-Naghdi results obtained by Ertekin & Kim (1998). The magnitude of the maximum deflection along the plate center and drift force are greater here than the Green-Naghdi results. This is likely due to the phase differences as observed in Fig. 4(b).

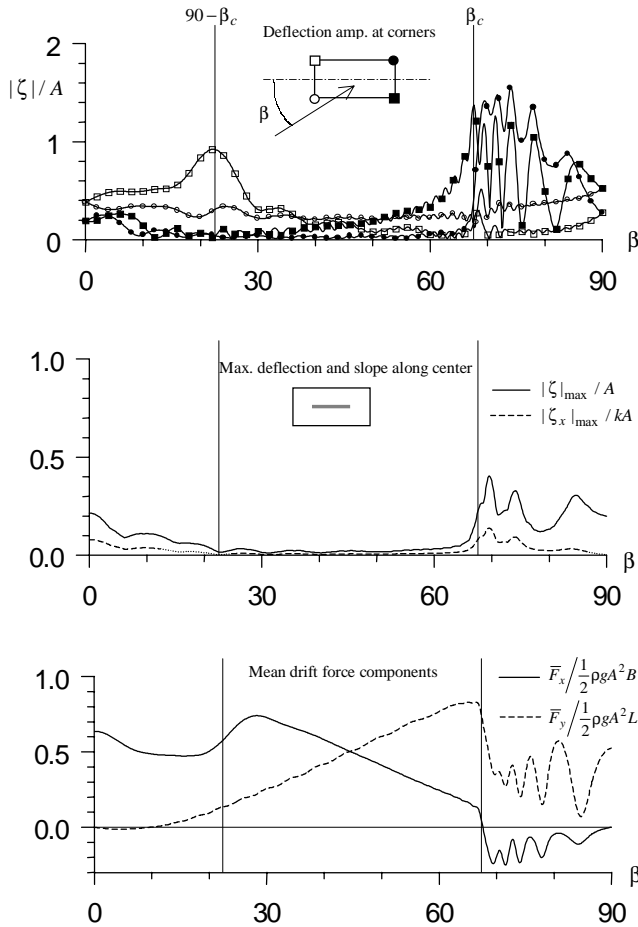


Fig. 9: Hydroelastic response and drift force of a 5 km-long VLFS in oblique seas.

The drift force results shown in Fig. 9 indicate that the transverse drift force becomes maximum at the critical angle and the longitudinal drift force becomes negative for $\beta > \beta_c$. The negative drift force results obtained here, and also by Ohmatsu (1998) for a different mat-type structure, can be explained by considering the reflected and transmitted wave patterns (see Ertekin & Kim (1998)).

And finally, we show some three-dimensional view of the results that display the effects of the L/λ ratio on the deflection amplitude and longitudinal drift force. In Fig. 10(a), the deflection RAO at the upper right corner ($x = L/2, y = B/2$) of the mat is shown. Clearly,

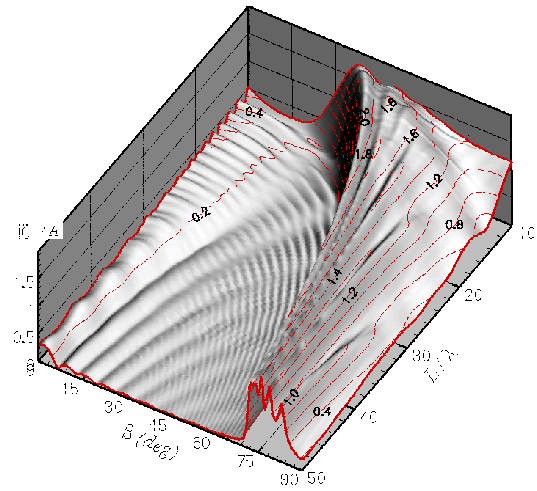
the response is larger in a wider range of wave angles when the L/λ ratio is smaller, *i.e.*, when the waves are longer. It is noted that the deflection RAO is quite large in some instances due to the rather low stiffness of the mat. Fig. 10(b) shows the maximum deflection RAO along the center of the mat. The cross section of the graph at $L/\lambda = 40$ was shown in the middle graph of Fig. 9. This maximum deflection is much smaller than the one in the upper right corner of the mat shown in Fig. 10(a). The negative drift forces in the x direction are visible in Fig. 10(c), and they cover a wider range of wave angles as the waves become longer. It is emphasized that the peaks of the hills in Fig. 10(a)-(b) and the cliff in Fig. 10(c) occur near the corresponding critical angles (see Kim & Ertekin (1998a)).

Acknowledgment: The material is based upon work supported by the U.S. National Science Foundation, Grant No. BES-9532037 and by the U.S. Office of Naval Research's MOB Program, through Float, Inc. The authors are grateful to Prof. Ronald W. Yeung for his invaluable discussions on the subject, and to Prof. Masashi Kashiwagi for kindly providing us with numerical data. SOEST Contribution No. 4708.

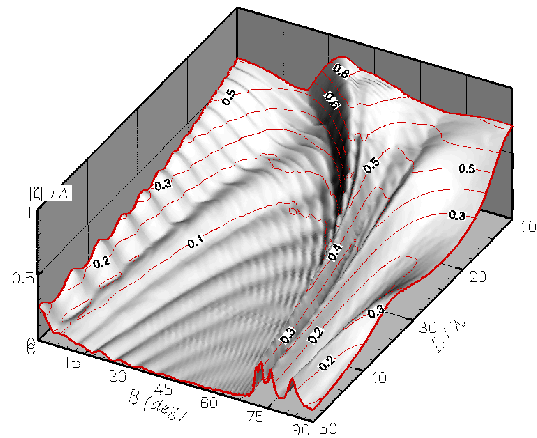
References

- ERTEKIN, R. C. AND KIM, J. W. 1998 Hydroelastic response of a mat-type structure in oblique, shallow-water waves. Submitted to. *J. Ship Res.*
- EVANS, D. V. AND DAVIES, T. V. 1968 Wave-ice interaction. Technical report. 1313. Davidson Lab., Stevens Inst. of Techno., Hoboken, N. J.
- FOX, C. AND SQUIRE, V. A. 1994 On the oblique reflexion and transmission of ocean waves at shore fast ice. *Phil. Trans. R. Soc. Lond.*, **347**, A, 185–218.
- IWAHASHI, Y., OHMATSU, S. AND TSUBOGA, T. 1998 Hydroelastic response characteristics of a pontoon type VLFS in waves (in Japanese). *Proceedings: SNAJ*, Vol. 183, 211–218.
- JOHN, F. 1950 On the motions of floating bodies, II. *Comm. Pure App. Math.*, **3**, 45–101.
- KASHIWAGI, M. 1998a A B-spline Galerkin scheme for calculating the hydroelastic response of a very large floating structure in waves. *J. Mar. Sci. Technol.*, **3**, 37–49.
- KASHIWAGI, M. 1998b A new solution method for hydroelastic problems of a very large floating structure in waves. *Proceedings: 17th Int. Conf. Off-shore Mechanics and Arctic Engineering*. ASME, OMAE98-4332, July, 8pp.
- KIM, J. W. AND ERTEKIN, R. C. 1998a Deformations of an infinitely-long, elastic plate floating in oblique waves: Linear Green-Naghdi theory. Submitted to. *J. Fluid Mech.*
- KIM, J. W. AND ERTEKIN, R. C. 1998b Wavemaker theory for a floating elastic plate: Hydroelastic response in beam seas. Submitted to. *Wave Motion*.

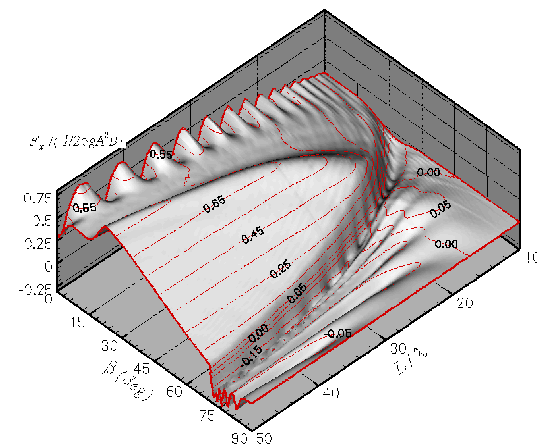
- MAMIDIPUDI, M. AND WEBSTER, W. C. 1994 The motions performance of a mat-like floating airport. In: *Hydroelasticity in Marine Technology*, O. M. FALTINSEN, Ed. Balkema Publishers, Rotterdam, pp 363–375.
- MARUO, H. 1960 The drift of a floating body on waves. *J. Ship Research*, **4**, 1–10.
- MEI, C. C. 1992 *The Applied Dynamics of Ocean Surface Waves*. World Scientific, 2nd printing, New Jersey.
- MEYLAN, M. AND SQUIRE, V. A. 1994 The response of ice floes to ocean waves. *J. Geophysical Res.*, **99**, C1, January 15, 891–900.
- NEWMAN, J. N. 1994 Wave effects on deformable bodies. *App. Ocean Res.*, **16**, 47–59.
- OHKUSU, M. AND NAMBA, Y. 1998 Hydroelastic behavior of floating artificial islands (in Japanese). *J. Soc. Naval Arch. Japan*, **183**, June, 239–248.
- OHKUSU, M. AND NAMBA, Y. 1996 Analysis of hydroelastic behavior of a large floating platform of thin plate configuration in waves. *Proceedings: Int. Workshop on Very Large Floating Structures, VLFS '96*, Hayama, Japan. 143–148.
- OHMATSU, S. 1998 Numerical calculation of hydroelastic behavior of pontoon type VLFS in waves. *Proceedings: 17th Int. Conf. on Offshore Mechanics and Arctic Engineering*. ASME, OMAE98-4333, July, 11pp.
- OHTA, M. AND OHMATSU, S. 1998 Analysis and experimental verification of elastic behavior of huge floating structure in waves (in Japanese). *Proceedings: 14th Ocean Engineering Symposium*. SNAJ, July, 475–481.
- RAYLEIGH, J. W. S. 1894 *The Theory of Sound*. Dover Publications (1945), New York.
- STOKER, J. J. 1957 *Water Waves: The Mathematical Theory with Applications*. New York: Interscience.
- WANG, S. Q., ERTEKIN, R. C. AND RIGGS, H. R. 1997 Computationally efficient techniques in the hydroelasticity analysis of very large floating structures. *Computers & Structures*, **62**, 4, 603–610.
- WEHAUSEN, J. V. AND LAITONE, E. V. 1960 *Surface Waves*, In *Handbuch der Physik*. Vol. 9. Springer-Verlag, Berlin. pp 446–778.
- WU, Y. S. 1984 Hydroelasticity of floating bodies. Doctoral dissertation, Brunel University, U.K. May.
- WU, Y. S., WANG, D., RIGGS, H. R. AND ERTEKIN, R. C. 1993 Composite singularity distribution method with application to hydroelasticity. *Marine Structures*, **6**, 143–163.
- YEUNG, R. W. AND BOUGER, Y. C. 1979 A hybrid integral-equation method for steady two-dimensional ship waves. *Int'l J. for Numer. Methods in Engr.*, **14**, 317–336.



(a) Deflection RAO at the upper right corner



(b) Maximum deflection RAO along the center



(c) Drift force RAO in the x direction

Fig. 10: Deflection and drift force RAOs as functions of wave angle and L/λ ratio for the 5-km-long mat.